

Check for updates

Unveiling the Mutual Promotion Mechanism of Adjacent Vacancy Defects Enables High-Performance Perovskite Solar Cells

Shujie Qu, Yiyi Li, Hao Huang,* Fu Yang, Changxu Sun, Qiang Zhang, Zhiwei Wang, Tongtong Jiang, Luyao Yan, Zhineng Lan, Yingying Yang, Peng Cui, Xicheng Ai, and Meicheng Li*

The perovskite defect evolution directly impacts the efficiency and stability of perovskite solar cells (PSCs). In this work, the mutual promotion mechanism of adjacent cation and anion vacancies in perovskite is unveiled, which means the cation/anion vacancy induces the adjacent anion/cation vacancy through decreasing the formation energy. This mutual promotion mechanism provides an explanation for the dynamic evolution of defects, and emphasizes the necessity of simultaneously passivating of adjacent defects. Accordingly, a new additive of 2-hydrazinylpyrazine is utilized to passivate adjacent defects, considering its adjacent electron-rich N atom, which can chemically bond uncoordinated Pb, and the hydrazine group, which can anchor FA+ through hydrogen bonds. Besides, this 2-hydrazinylpyrazine also optimizes the perovskite crystallization through accelerating nucleation and slowing crystal growth, demonstrated by the in situ photoluminescence spectra. The resulting inverted 0.08 cm² and 1 cm² PSCs obtain PCEs of 26.28% and 24.71%, respectively. Moreover, the Target device shows enhanced stability by maintaining 93% and 90% of the initial efficiency after operating 1700 h under 1-sun illumination and being exposed to harsh thermal cycling for 150 times, respectively.

1. Introduction

Metal halide perovskite solar cells (PSCs) have achieved certificated efficiency of 27.0% in a single-junction structure, which establishes them as a highly promising technology to spearhead the

S. Qu, H. Huang, F. Yang, C. Sun, Q. Zhang, Z. Wang, T. Jiang, L. Yan, Z. Lan, Y. Yang, P. Cui, M. Li

State Key Laboratory of Alternate Electrical Power System with Renewable Energy Sources

North China Electric Power University

Beijing 102206, China

E-mail: hhuang@ncepu.edu.cn; mcli@ncepu.edu.cn

Y. Li, X. A

Key Laboratory of Advanced Light Conversion Materials and Biophotonics School of Chemistry and Life Resources Institution Renmin University of China

Beijing 100872, China

D

The ORCID identification number(s) for the author(s) of this article can be found under https://doi.org/10.1002/adma.202508643

DOI: 10.1002/adma.202508643

photovoltaic revolution.[1-7] However, they are still facing challenges of PSCs, including the gap between the current efficiency and the theoretical Shockley-Queisser (S-O) values, the unsatisfactory device stability, especially under the stressed applied conditions, and the scale-up efficiency loss. These challenges are badly influenced by the perovskite defects, considering that the defects can cause nonradiative carrier recombination and accelerate the ion migration and phase transition. Hence, the research regarding the defect evolution and the corresponding modulation strategy is essential for pursuing high-quality perovskite, thus contributing to the high-efficiency and stable PSCs.[8]

As for the popular perovskite material of $FAPbI_3$ (FA is formamidinium), the defects of V_I and V_{FA} are the common defects due to the weak I-Pb bonding and interaction between FA^+ with the $[PbI_6]^{4-}$. These defects also become the focus object of research to modulate

film properties, suppress ion migration, and improve device photovoltaic performance.^[10] Using halogens, pseudo-halogen anions such as thiocyanate and acetate, as well as phosphorus (P)-containing, nitrogen (N)-containing, and sulfur (S)containing Lewis base molecules to passivate V_I have been reported to be feasible approaches. In 2023, S-containing 3(methylthio)propylaminehydroiodide had been used to passivate V₁ through chemical bonding uncoordinated Pb atom via an electron-rich S atom.[11] This direct filling-manner passivation approach of $V_{\scriptscriptstyle I}$ also works for $V_{\scriptscriptstyle FA}$. Considering the similar molecular size, ammonium-, amidine-, and guanidine- salts have normally been utilized to passivate V_{FA} . For example, propylphosphonic acid 3-ammonium bromide (PPAABr) has been utilized to fill the FA+ vacancy on the perovskite surface, contributing to achieving high-efficiency HTL-free inverted PSCs.[12] Except from the manner of filling the vacancy, anchoring the I⁻ or FA⁺ can also reduce the vacancy defects since the anchoring effect can increase the defect formation energy. Hydrogen bonding of I···H was normally utilized to stabilize I-, and hydrogen bonding of N···H or cation– π interaction was utilized to stabilize cations. For

www.advancedsciencenews.com

ADVANCED MATERIALS

www.advmat.de

15214955, 2025, 40, Downloaded from https://alvanced.online/brary.wiley.com/doi/10.1002/adma.2025/08643 by North China Electric Power University Beijing, Wiley.com/min.brary.wiley.com/mi

example, polyhexamethyleneguanidine hydrochloride was incorporated into perovskite to anchor FA $^+$ through multiple hydrogen bonds with an absorption energy of -3.47 eV, which increases the formation energy of $V_{\rm FA}$ from 1.29 to 1.94 eV, thereby reducing the $V_{\rm FA}$ defect and improving the device photovoltaic performance. $^{[13]}$

Considering the high density of both V_I and V_{EA} in perovskite, researchers attempt to synchronously passivate both defects using a suitable additive or an additive group. Guanabenz acetate salt was reported to passivate both cation and anion vacancies, which blocks the perovskite hydration and allows the crystallization of a high-quality film in ambient air.[14] Recently, A tripleadditive strategy was utilized to passivate perovskite defects and regulate crystallization, which improved the efficiency and stability of PSCs. [15] Although the above strategy shows a positive effect on passivating both the vacancy defects, the issue of adjacent vacancy defects was important but normally ignored, especially considering the inevitable influence of vacancy defects on their adjacent site. There are reports to passivate the adjacent defects using a multi-binding site additive, which mainly focuses on the adjacent V_I defects. A deeper understanding of the interinfluence of adjacent cation and anion vacancy defects and its guidance for the selection or design of additives that work for adjacent vacancy defects is still urgently needed.

Herein, we explored the inter-influence of the adjacent cation and anion vacancies in perovskite using the theoretical calculation of density functional theory (DFT) and ab initio molecular dynamics (AIMD). We revealed the mutual promotion mechanism of adjacent cation and anion vacancies, which means the V_I will accelerate the formation of adjacent V_{FA} through decreasing its formation energy from 2.80 to 1.41 eV, and the V_{FA} will accelerate the formation of adjacent V_I through decreasing its formation energy from 1.54 to 1.19 eV. This mutual promotion mechanism inspired us to further utilize the 2-hydrazinylpyrazine (2-HZP) to passivate adjacent cation and anion vacancies, considering its adjacent electron-rich N atom, which can chemically bond to uncoordinated Pb and hydrazine group, which can form hydrogen bonds with FA+. In addition, the 2-HZP can accelerate the perovskite nucleation and slow the crystal growth, contributing to a perovskite film with enhanced crystallinity. Owing to the well-passivated defects and optimized perovskite crystallization, the inverted 0.08 cm² PSCs and 1 cm² PSCs achieved PCEs of 26.28% and 24.71%, respectively. The regulated PSCs also obtained a PCE of 25.80%. Moreover, the device with 2-HZP shows enhanced stability by suppressing ion migration. After 1700 h of operation under 1-sun illumination, the device can retain 93% of its initial efficiency.

2. Results and Discussion

2.1. Mutual Promotion Mechanism of Adjacent Cation and Anion Vacancies

As a soft ionic crystal, the defect evolution and lattice deformation are inevitably influenced by their surroundings, including the adjacent atom and defects.^[16] To explore the inter-influence of adjacent anion and cation vacancies in perovskite, we carried out the theoretical research using the calculation of density functional theory (DFT) and ab initio molecular dynamics (AIMD).^[17]

Based on the relaxed lattice model of FAPbI3, the defect formation energy of a $V_{\rm I}$ is calculated to be 1.54 eV (Figure 1a). Notably, when there exists an adjacent V_{FA}, the defect formation energy of V_I decreases to 1.19 eV (Figure 1b), suggesting that the presence of V_{FA} facilitates the formation of adjacent V_{I} (Figure 1c). This phenomenon may arise from the diminished binding stabilization of anions induced by cation vacancies. Specifically, the absence of FA⁺ disturbs the local bonding environment and electrostatic balance, leading to slight distortion of the PbI6 octahedral framework and weakening the binding of nearby I- ions, thereby facilitating subsequent vacancy formation.^[2,18,19] Correspondingly, we also calculated the defect formation energy of V_{FA} in the intact FAPbI₃ lattice to be 2.80 eV (Figure 1d), indicating that V_{FA} is generally difficult to form under equilibrium conditions. However, when an adjacent V_I is introduced (Figure 1e), the formation energy of $V_{\scriptscriptstyle {\rm FA}}$ drastically decreases to 1.41 eV. This marked reduction may be attributed to the collapse of the Pb-I octahedral confinement caused by V₁, which weakens the structural integrity, thereby promoting cation escape from the lattice. The facilitation effects of V_I on the adjacent V_{FA} were illustrated in Figure 1f. We reveal that the cation/anion vacancy induces the adjacent anion/cation vacancy through decreasing the formation energy, which we describe as the mutual promotion mechanism of adjacent anion and cation vacancies. To validate the completeness of the mechanism, we also evaluated representative anti-site defects, such as Pb substituting I (Pb_I) and I substituting FA (I_{FA}). As shown in Figure S1 (Supporting Information), these anti-site defects exhibit relatively high formation energies, which indirectly suggests that the mutual promotion between adjacent anion and cation vacancies is energetically more favorable.

To further elucidate the mutual promotion mechanism between adjacent cation and anion vacancies, we performed AIMD simulations.^[20] To quantitatively assess the thermodynamic and kinetic feasibility of defect generation, we specifically focus on the ion migration energy barrier (E_a), a critical physical parameter that assists the defect formation energy discussed above to evaluate the defect formation property. As shown in Figures 2a,b, the AIMD-simulated migration processes of FA⁺ and I⁻ ions were performed based on two distinct configurations without/with adjacent V_I/V_{EA} defects. Both configurations enable direct visualization of ion migration pathways. As shown in Figure 2c, the presence of adjacent V_I reduces the migration energy barrier of FA $^+$ from 0.71 to 0.31 eV. Similarly, the adjacent $V_{\rm FA}$ decreases the migration energy barrier of I- from 0.42 to 0.22 eV (Figure 2d). This reduction in the migration energy barrier of FA+ or I- under different conditions well aligns with the DFT calculation results discussed earlier. Furthermore, we performed an analysis of ion migration rates using the Formula: $k \propto e^{-E_a/k_bT}$, where the k_h and T represent the Boltzmann constant and reaction temperature, respectively. As shown in Figure 2e,f, both FA⁺ and I - exhibit identical trends under two thermodynamic conditions (298.15 and 320 K): adjacent vacancy defects substantially accelerate their migration rates, respectively. In short, from the results of both the calculation of DFT and AIMD, we reveal that the vacancy defect formation is accelerated by its adjacent vacancy defects, which highlights the necessity for the synchronous passivation of both adjacent cation and anion vacancies for the fabrication of high-quality perovskite film.

15214095, 2025

com/doi/10.1002/adma.202508643 by North China Electric Power University Beijing, Wiley Online Library on [14/10/2025]. See the Terms

and-conditions) on Wiley Online Library for rules of use; OA articles are governed by the applicable Creative Commons

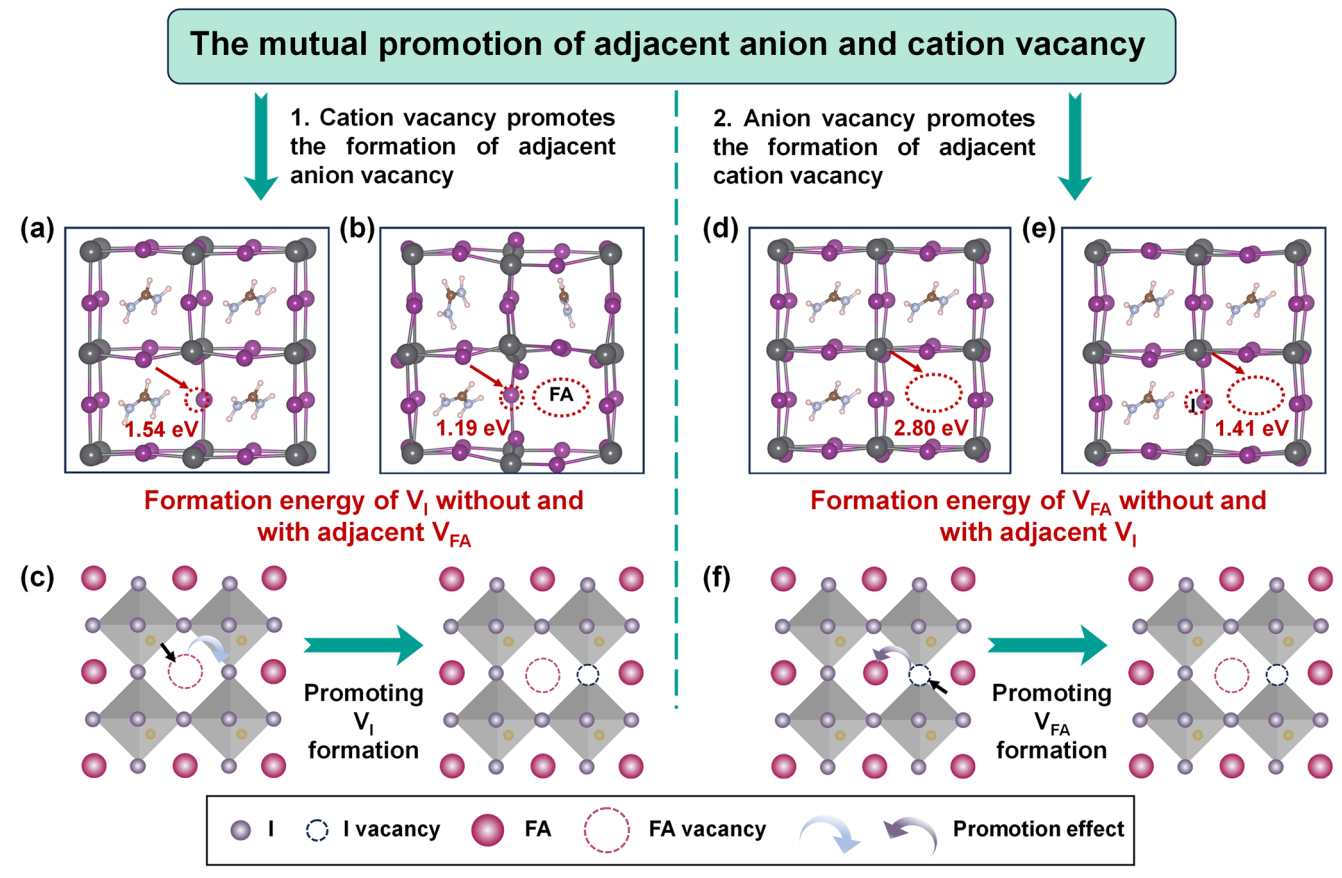


Figure 1. Mutual promotion model of adjacent cation and anion vacancies a,b) Defect formation energy results of V_I . c) Schematic illustration of cation vacancy promoting anion vacancy formation. d,e) Defect formation energy results of V_{FA} . f) Schematic illustration of anion vacancy promoting cation vacancy formation.

Based on these findings, we attempt to passivate both the adjacent defects simultaneously. Considering the suitable molecular size and functional group or atom, the 2-hydrazinylpyrazine (2-HZP, molecular structure shown in Figure S2, Supporting Information) was utilized to serve as the passivator, since its adjacent electron-rich N atom which can chemical bond uncoordinated Pb, and hydrazine group which can form hydrogen bonds with FA⁺ (Figure 2g). We validated this double-site interaction between 2-HZP and perovskite using DFT calculations. As shown in Figure 2h, the calculated binding energy between 2-HZP and perovskite in a manner of N atom interacting with uncoordinated Pb and hydrazine group forming hydrogen bonds with FA⁺ to be -1.22 eV, which confirms the feasibility and reliability of this interaction. After being passivated by 2-HZP, subsequent DFT and AIMD analyses reveal that the formation energy of V_{FA} increases from 1.41 to 4.84 eV, accompanied by a rise in the FA+ migration energy barrier from 0.31 to 0.91 eV (Figure 2i). In this case, the formation energy of the neighboring V_I adjacent to FA⁺ increases from 1.19 to 3.00 eV, while the migration energy barrier rises from 0.22 to 0.56 eV. (Figure \$3, Supporting Information) These results theoretically demonstrate the feasibility of 2-HZP on passivating adjacent vacancy defects.

Based on the aforementioned mentioned mutual promotion model of adjacent cation and anion, 2-HZP is employed and has been theoretically demonstrated to passivate adjacent vacancy defects. We first explored the concentration of 2-HZP, and as shown in Figure S4 (Supporting Information), the optimal concentration was determined to be 0.3 mol%. We also attempted to identify molecular candidates capable of directly filling V_{FA} , and selected pyrazine-2-carboxamidine hydrochloride (PZCA) for verification. As shown in Note S1 and Figures S5 and S6 (Supporting Information), although PZCA exhibits a certain degree of defect passivation, the device performance remains inferior to that achieved with 2-HZP. To validate this hypothesis experimentally, we designed a series of characterizations to investigate the interaction between 2-HZP and perovskite. For clarity in identification, films or devices incorporating 2-HZP are designated as Target, whereas their counterparts without 2-HZP are labeled as Normal. Firstly, to investigate the interaction between the 2-HZP and FA⁺, Fourier transform infrared spectroscopy (FTIR) analysis was performed. As shown in Figure 3a,b, after the incorporation of 2-HZP, the N-H stretching vibration peak of FA⁺ shifts from 3395 to 3415 cm $^{-1}$, and the C = N stretching vibration peak shifts from 1720 to 1716 cm₋₁, indicating the formation of hydrogen bonds between 2-HZP and FA⁺.[21,22] To investigate the interaction between 2-HZP with [PbI₆]⁴⁻ octahedral, X-ray photoelectron spectroscopy (XPS) characterization was conducted, with results shown in Figure 3c. The Pb 4f doublet peaks at 143.4 and 138.5 eV exhibit a distinct shift toward lower binding energy $(\Delta E = -0.3 \text{ eV})$ in the Target film compared to the Normal film.

15214095, 2025, 40, Downloaded from https://advanced.

onlinelibrary.wiley.com/doi/0.1002/aha.m.2020/8643 by North China Electric Power University Bejing. Wiley Online Library on [1410/2025]. See the Terms and Conditions (https://onlinelibrary.wiley.com/terms-and-conditions) on Wiley Online Library for rules of use; OA articles are governed by the applicable Creative Commons Licensea

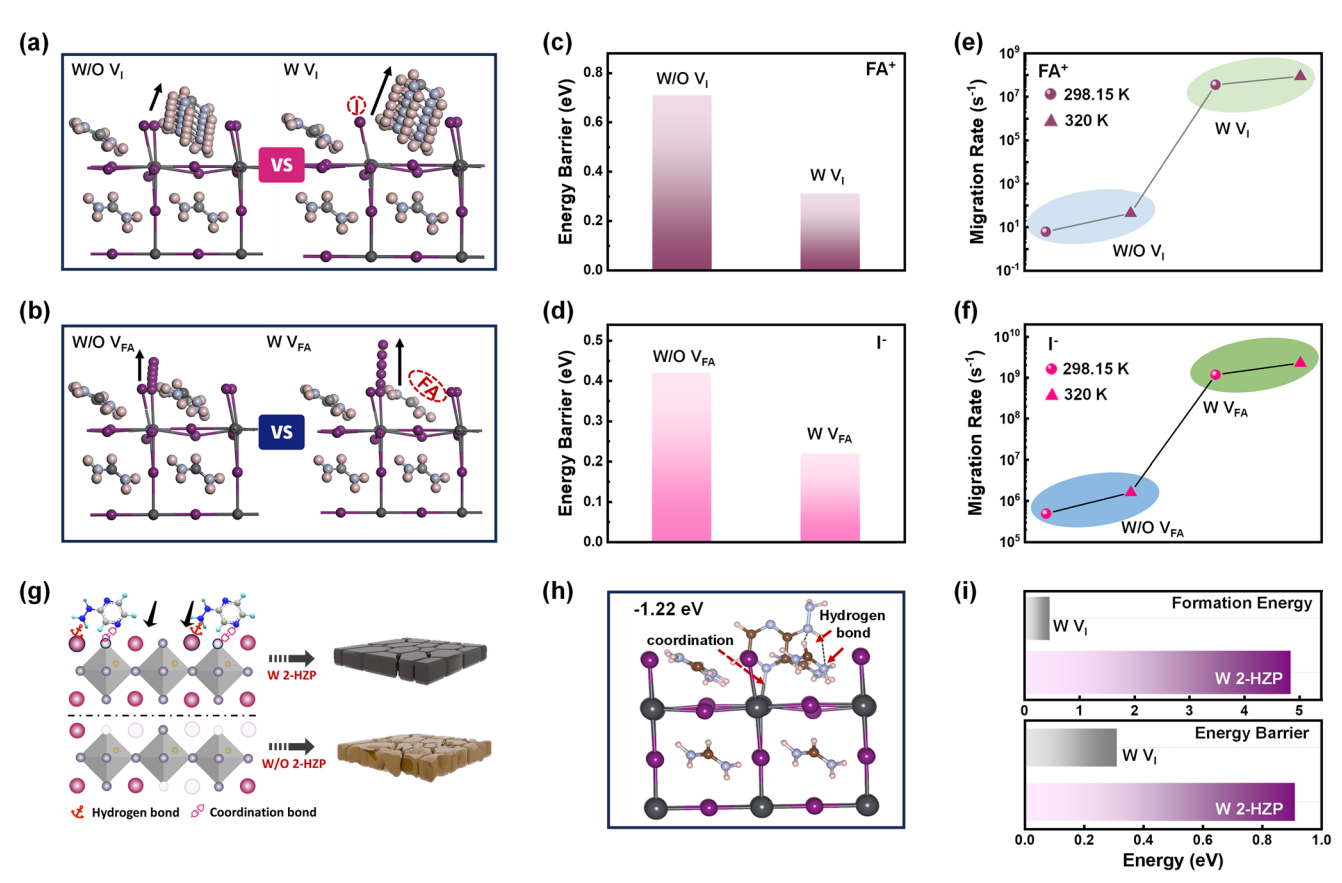


Figure 2. Mutual promotion mechanism of adjacent cation and anion vacancies a,b) Schematic illustration of AIMD. c) Migration energy barrier of FA $^+$. d) Migration energy barrier of I $^-$. e) Migration rate of FA $^+$. f) Migration rate of I $^-$. g) Schematic diagram of defect passivation for 2-HZP. h) DFT results of 2-HZP and perovskite. i) Defect formation energy of V_{FA} and migration energy barrier of FA $^+$.

This phenomenon is attributed to the increased electron density of Pb²⁺, which originates from the passivation of uncoordinated Pb defects through Pb-N interaction, where the N atom is derived from the heterocyclic ring of the 2-HZP molecule, as confirmed by our DFT calculations.^[23,24] Hence, the interaction between 2-HZP and perovskite, as revealed through different experimental measurements, aligns consistently with the theoretical insights derived from the DFT and AIMD calculations.

The defect states of the perovskite film are further explored through various experiments to validate the passivation effects of 2-HZP. Firstly, Hole-only/electron-only devices were fabricated for space-charge-limited current (SCLC) measurements to estimate the defect density of perovskite films.^[25,26] The defect density $(N_{\rm trap})$ of the perovskite film can be calculated using the formula: $N_{\rm trap} = 2\epsilon_{\rm r}\epsilon_0 V_{\rm TFL}/eL^2$, where $\epsilon_{\rm r}$ is the relative permittivity, ε_0 is the vacuum permittivity, e is the elementary charge, V_{TFL} is the trap-filling limit voltage, and L is the thickness of the perovskite film (Figures S7 and S8, Supporting Information). Based on the electron-only device, the calculated $N_{\rm trap}$ of perovskite films decreased from 1.6 $\times~10^{16}~cm^{-3}$ to 1.1 $\times~10^{16}~cm^{-3}$ after incorporating 2-HZP (Figure 3d). Based on the hole-only device, the calculated $N_{\rm trap}$ of perovskite films decreased from 0.9×10^{16} cm⁻³ to 0.5×10^{16} cm⁻³ after incorporating 2-HZP (Figure 3d). In the following, the trap density of states (tDOS) distribution within PSCs is analyzed using admittance spectroscopy.^[27-29] This distribution can be quantified mathematically through the formalism presented below: $-\omega V_{\rm bi}/{\rm qk_B}TW\times {\rm d}C/{\rm d}\omega,$ where $V_{\rm bi}$ is the built-in potential, W is the depletion width, q is the elementary charge, C is the capacitance, and ω is the applied angular frequency. As shown in Figure 3e, compared to the Normal device, the Target device shows an obvious reduction of defect density, which is consistent with the results of SCLC measurements.

Optoelectronic characterization was also employed to further investigate the defect passivation effect of 2-HZP on perovskite films. As demonstrated in Figure 3f,g, the Target film exhibits significantly higher photoluminescence (PL) intensity compared to the Normal film. Furthermore, time-resolved photoluminescence (TRPL) measurements (Figure S9, Supporting Information) corroborate this observation, revealing a substantially longer carrier lifetime of 3.94 µs for the Target film, in contrast to the 1.32 µs of the Normal film.[30,31] In addition, the femtosecond transient absorption spectroscopy (TAS) was performed on both Normal and Target films. As shown in Figure 3h,i, both films were irradiated with the same pump source, and a distinct photobleaching (PB) negative signal of the perovskite was observed. Notably, the Target film exhibits stronger PB intensity and slower decay kinetics compared to the Normal film (Figure \$10, Supporting Information), indicating enhanced charge carrier lifetimes and reduced defectmediated non-radiative recombination.[32,33] These results of

15214095, 2025, 40, Downloaded from https://advanced.onlinelibrary.wiley.com/doi/10.1002/adma.202508643 by North China Electric Power University Beijing, Wiley Online Library on [14/10/2025]. See the Terms

and-conditions) on Wiley Online Library for rules of use; OA articles are governed by the applicable Creative Commons License

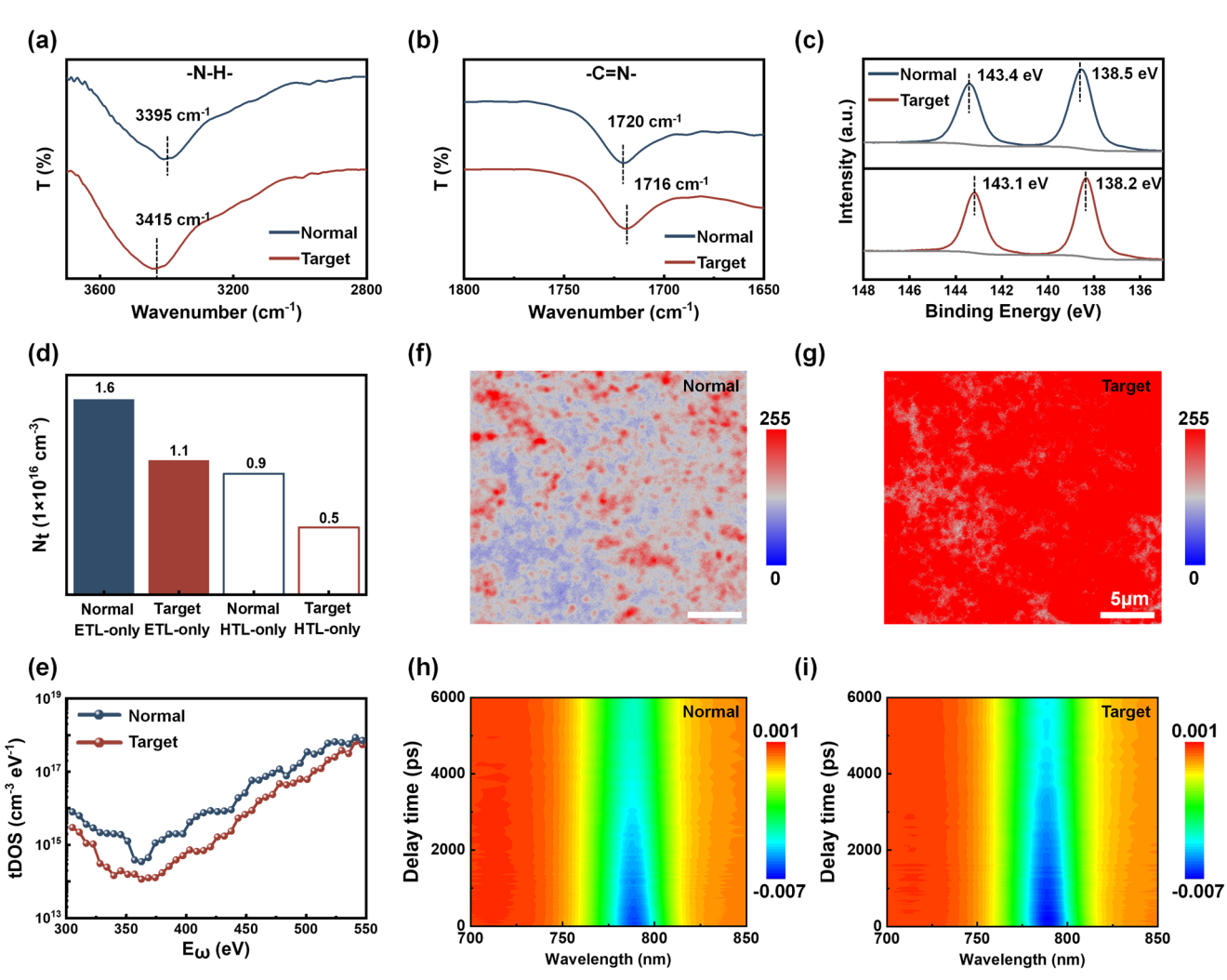


Figure 3. Effective multi-defects management of 2-HZP a,b) FTIR spectra of the Normal and Target films. c) Pb 4f XPS spectra of the Normal and Target films. d) N_{trap} results of the Normal and Target devices. e) tDOS results of the Normal and Target devices. f,g) PL mapping images of the Normal and Target films. h,i) Transient absorption studies of the Normal and Target films.

optoelectronic measurements collectively demonstrate that the 2-HZP can effectively passivate the perovskite defects, contributing to the suppressed non-radiative recombination and improved charge carrier dynamics charge carrier dynamics.

2.2. Assisted Crystallization of Perovskite Film

Considering the interaction between 2-HZP with FA $^+$ and $[PbI_6]^{4-}$ octahedral, respectively, we speculate that 2-HZP also shows an influence on perovskite crystallization. Firstly, we performed the in situ PL characterization to make an in-depth investigation of the crystallization process. The entire perovskite crystallization process can be divided into two stages, the stage I corresponds to the spin-coating process, which spans from the spin-coating of the perovskite precursor solution to the completion of antisolvent drip-coating, the stage II corresponds to the perovskite annealing process. As illustrated in **Figures 4a**,b, a distinct PL signal emergence is observed upon antisolvent drip-

coating completion, which should be attributed to the incipient perovskite nucleation due to the rapid extraction of DMSO/DMF solvents. In detail, the Target sample exhibits enhanced nucleation dynamics during this critical phase, as evidenced by its intensified PL response. The enhanced nucleation kinetics principally originate from the incorporation of 2-HZP, which operates through dual mechanistic pathways: hydrogen-bonding interactions with FA+ cations (as previously demonstrated) stabilize the ionic arrangement in the precursor matrix by suppressing stochastic molecular fluctuations, thereby reducing dissociation of minor molecular clusters while promoting the assembly of larger supramolecular aggregates; simultaneously, its competitive coordination with Pb2+ ions disrupts the solvent (DMSO/DMF)-metal coordination equilibrium, effectively lowering the energy barrier for [PbI₆]⁴⁻ octahedral assembly and accelerating the formation of thermodynamically stable crystalline nuclei.[21,34] The Dynamic Light Scattering (DLS) analysis (Figure S11, Supporting Information) reveals the presence of noticeably larger aggregates in the Target sample, indicating that 2-HZP

15214095, 2025, 40, Downloaded from https://advanced.

onlinelibrary.wiley.com/doi/0.1002/aha.m.2020/8643 by North China Electric Power University Bejing. Wiley Online Library on [1410/2025]. See the Terms and Conditions (https://onlinelibrary.wiley.com/terms-and-conditions) on Wiley Online Library for rules of use; OA articles are governed by the applicable Creative Commons Licensea

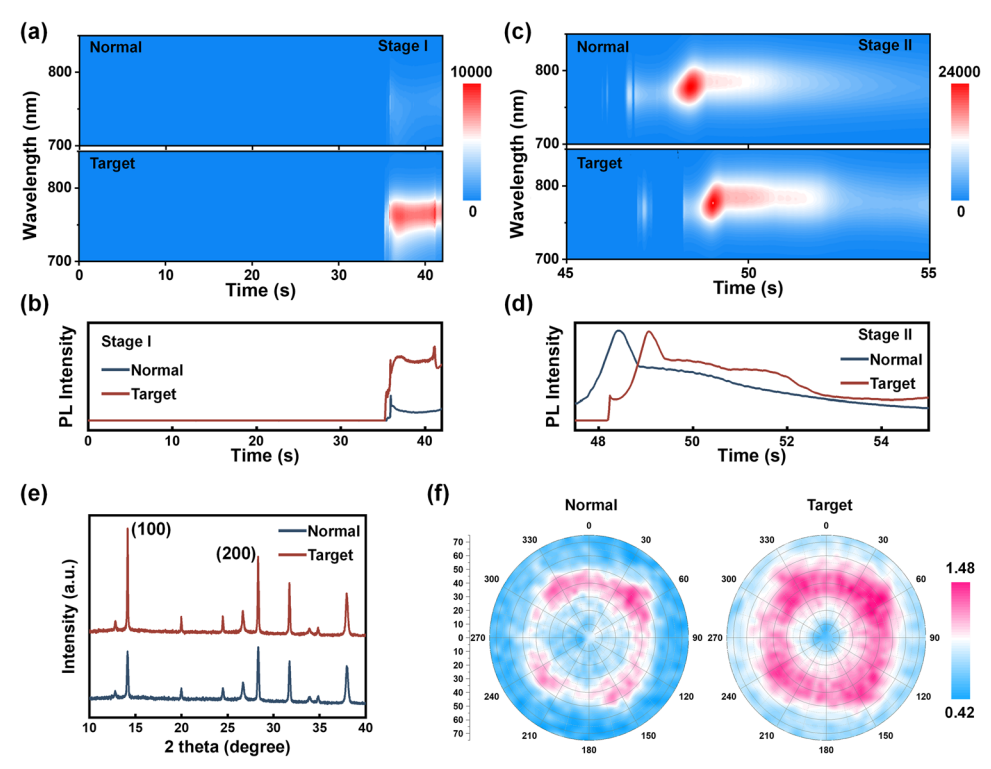


Figure 4. Crystallization regulation of 2-HZP on perovskite films a-d) In situ PL spectra of Normal and Target perovskite films during different stages. e) XRD spectra of the Normal and Target films. f) Pole figure of the (100) diffraction peak.

promotes the formation of more stable supramolecular assemblies by suppressing molecular fluctuations.^[35]

In Stage II, in situ PL via Figure 4c,d reveals instantaneous crystallization kinetics upon hot-plate contact, manifested by a rapid PL intensity surge. While both Normal and Target samples exhibit parallel temporal evolution patterns in PL progression, this mechanistic convergence confirms that crystallization dynamics at this stage are predominantly dictated by the abrupt thermal input. Subsequent to the initial PL surge, a marked quenching phenomenon emerges, characterized by rapid signal attenuation attributable to solvent evaporation-induced phase transition dynamics, which governs the morphological stabilization from wet film to solid film. Following this phase, the Target film exhibited a longer crystallization process, indicating that the crystal restructuring in the Target film is slower and more complete than that in the Normal film. Further investigation of the subsequent film growth phase (Stage III, Figure S12, Supporting Information) reveals distinct PL evolution patterns: Normal film exhibits a continuous PL quenching trend, whereas Target film demonstrates an initial transient intensity decline followed by a sustained intensity recovery, ultimately achieving superior emission stability compared to the Normal sample. This divergence is attributed to the defect passivation capability of 2-HZP, which effectively mitigates non-radiative recombination and optimizes the perovskite film.

X-ray diffraction (XRD) characterization was further conducted to characterize the perovskite film. As evidenced by Figure 4e, the Target film exhibits an enhanced (100)/(200) orientation, with a significant enhancement in crystallization intensity. This preferred orientation is further corroborated by the (100)-

plane pole Figure analysis (Figure 4f), which demonstrates significantly intensified diffraction signatures in the Target film.[36] This improvement in crystallization is further supported by the UV-vis absorption spectra (Figure \$13, Supporting Information), where the Target film exhibits slightly higher absorption than the Normal film, particularly in the 450-550 nm range. Surface morphology of the perovskite film was also investigated using scanning electron microscopy (SEM). As shown in Figure S14 (Supporting Information), at different scales, the Target film exhibits a smoother and more uniform surface, which indicates the optimized crystallization after incorporating 2-HZP. Meanwhile, the films on TiO2 substrates, the electron transport layers normally applied in regular PSCs, were also characterized using Atomic Force Microscope (AFM) (Figure \$15, Supporting Information), delivering a smoother surface morphology with reduced surface roughness after incorporating 2-HZP, which validates the optimized crystallization.

2.3. Photovoltaic Performance of PSCs

Based on the demonstrated advantages of 2-HZP in defect passivation and crystallization modulation, we fabricated PSCs with the structure of Fluorine-doped tin oxide (FTO)/[4-(3,6-Dimethoxy-9H-carbazol-9-yl)butyl]phosphonic Acid (MeO-4PACZ)/Perovskite/PEAI/[6,6]-Phenyl C_{61} butyric acid methyl ester (PCBM)/2,9-dimethyl-4,7-diphenyl-1,10-phenanthrolin (BCP)/Ag and further investigated the influence of 2-HZP on the photovoltaic performance. Before characterizing the device efficiency, the device's physical property was characterized

15214095, 2025

mlinelibrary.wiley.com/doi/10.1002/adma.202508643 by North China Electric Power University Beijing, Wiley Online Library on [14/10/2025]. See the Terms

on Wiley Online Library for rules of use; OA articles are governed by the applicable Creative Commons

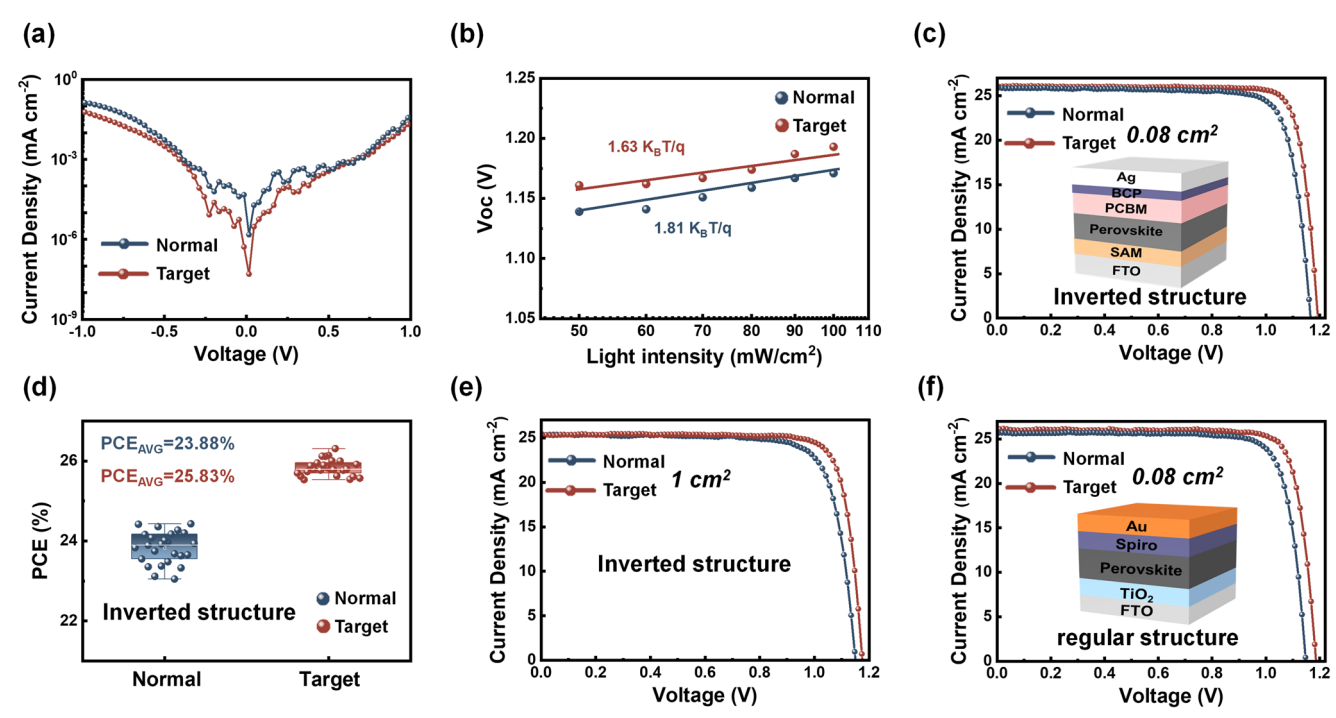


Figure 5. Photovoltaic performance of PSCs a) Dark *J-V* curves of the Normal and Target PSCs. b) The dependence of V_{OC} on the light intensity of Normal and Target PSCs. c) *J-V* curves of Normal and Target PSCs with an active area of 0.08 cm² (inverted structure). d) Distribution of the PCE values of the 25 Normal and Target PSCs. e) *J-V* curves of Normal and Target PSCs with an active area of 1 cm² (inverted structure). f) *J-V* curves of Normal and Target PSCs with an active area of 0.08 cm² (regular structure).

through measuring dark current and ideality factor ($\eta_{\rm ID}$). As shown in **Figure 5a**, the Target PSC exhibits significantly suppressed dark saturation current density (J_0), which is primarily attributed to the reduced non-radiative recombination resulting from the defect passivation of 2-HZP. The open-circuit voltage versus light intensity relationship was analyzed using the equation $V_{\rm OC} = (\eta_{\rm ID} k_{\rm B} T/q)^* \ln(I)$, where $k_{\rm B}$ is the Boltzmann constant and q denotes the elementary charge. The calculated $\eta_{\rm ID}$ for Normal and Target PSCs are 1.81 and 1.63, respectively (Figure 5b). The lower $\eta_{\rm ID}$ value in Target PSC indicates suppressed trap-assisted recombination, consistent with the reduced dark current observed in prior measurements. These results substantiate that the introduction of 2-HZP is supposed to contribute to the efficiency improvement of PSCs.

We statistically analyzed photovoltaic parameters from 25 independently fabricated devices for both Normal and Target PSCs. As shown in Figure 5c, the champion Target PSC achieves a PCE of 26.28% ($J_{SC} = 26.02 \text{ mA cm}^{-2}$, $V_{OC} = 1.193 \text{ V}$, FF = 84.65%) with negligible hysteresis (Table S1, Supporting Information), demonstrating a marked improvement over the Normal PSC performance of 24.44% ($J_{SC} = 25.89 \text{ mA cm}^{-2}$, $V_{OC} = 1.161 \text{ V}$, FF = 81.31%). The external quantum efficiency (EQE) spectrum (Figure \$16, Supporting Information) yields an integrated shortcircuit current density of 25.72 mA cm⁻², showing a small variation from the values obtained from current density-voltage (I-V) measurements. Notably, as shown in Figure 5d, the PCE distribution histograms demonstrate good reproducibility for both device types, with Target PSCs achieving an average PCE of 25.83%, significantly surpassing the average efficiency (23.88%) of Normal PSCs. The corresponding distribution histograms of additional

photovoltaic parameters, including $V_{\rm OC}$, $J_{\rm SC}$, and FF, are provided in Figure S17 (Supporting Information). We also validated the reproducibility of 2-HZP by testing PSCs from different fabrication batches, as shown in Figure S18 (Supporting Information).

To validate the scalability of 2-HZP, we further fabricated inverted PSCs with an active area of 1 cm2. Notably, as shown in Figure 5e, the Target PSC achieves a PCE of 24.71% (I_{SC} = 25.33 mA cm⁻², $V_{\text{OC}} = 1.174 \text{ V}$, FF = 83.08%, Table S2, Supporting Information), surpassing the Normal PSC efficiency of 22.95% ($J_{SC} = 25.39 \text{ mA cm}^{-2}$, $V_{OC} = 1.147 \text{ V}$, FF = 78.79%). In addition, the performance parameters of the additional 10 Target devices are shown in Table S3 (Supporting Information), exhibiting a satisfying reproducibility. In this study, unless otherwise specified, all characterizations were conducted on inverted structure devices. To further validate the reliability and universality of 2-HZP for improving PSC efficiency, we implemented this additive in regular structure devices with the architecture FTO/TiO₂/PVK/4-MeO-PEAI/Spiro/Au. As illustrated in Figure \$19 (Supporting Information), the PCE distribution of 25 independent devices demonstrates that the Target PSC achieves an average PCE of 25.33%, which is higher than that (23.34%) of Normal PSC devices. Encouragingly, the Target PSC achieves a champion PCE of 25.80%, with a I_{SC} of 26.09 mA cm⁻², a V_{OC} of 1.182 V, and an FF of 83.65% (Figure 5f; Table S4, Supporting Information). This performance surpasses that of the Normal PSC, which has a PCE of 24.32%, with a J_{SC} of 25.97 mA cm⁻², a $V_{\rm OC}$ of 1.174 V, and an FF of 79.79%. Moreover, we also validated the effect of 2-HZP in a regular device structure using MAPbI₃ as the perovskite composition. As shown in Figure S20 (Supporting Information), the Target PSCs exhibited significantly

15214095, 2025, 40, Downloaded from https://advancec

onlinelibrary.wiley.com/doi/10.1002/adma.202508643 by North China Electric Power University Beijing, Wiley Online Library on [14/10/2025]. See the Terms

and-conditions) on Wiley Online Library for rules of use; OA articles are governed by the applicable Creative Commons License

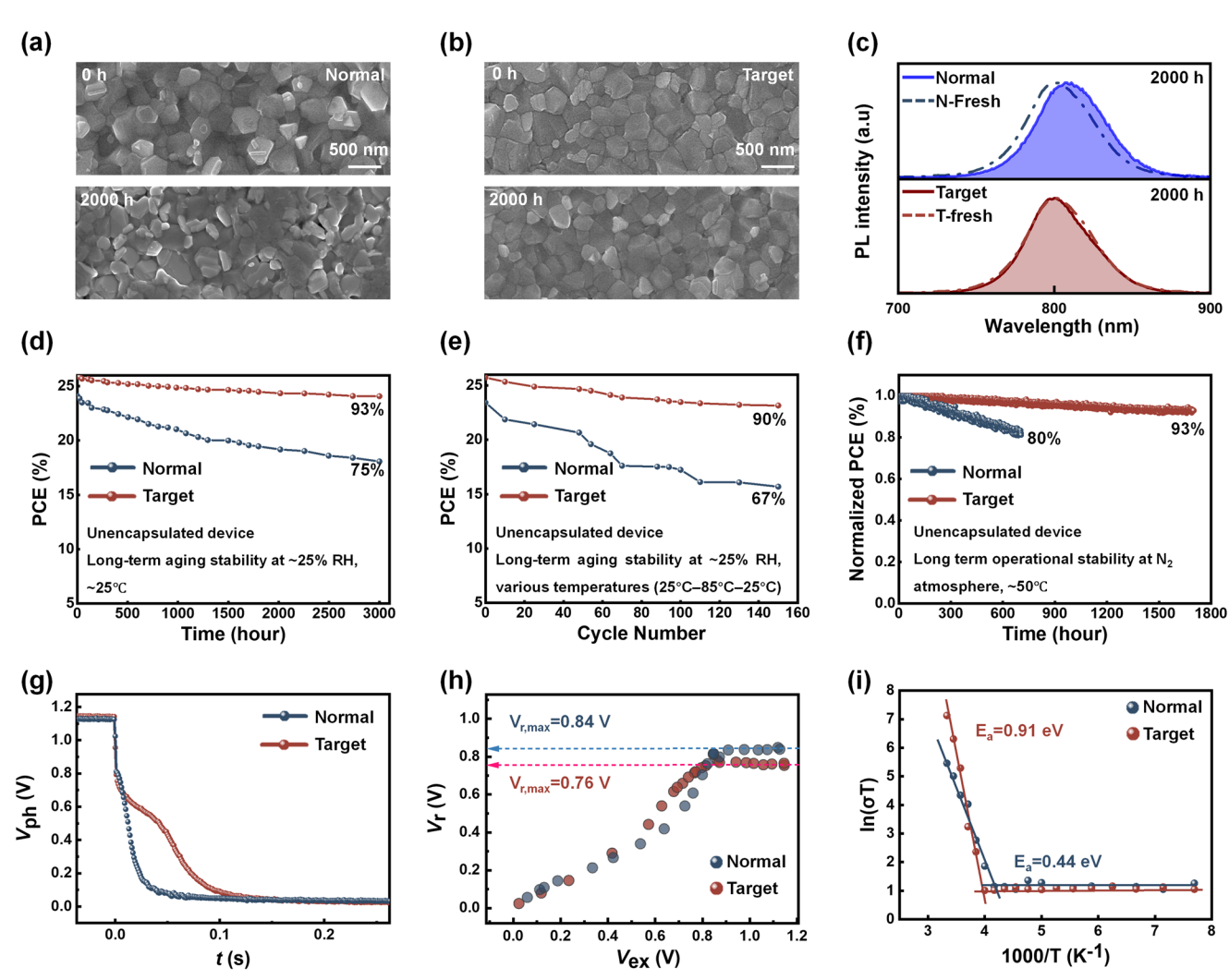


Figure 6. Stability performance and ion migration a,b) SEM images and c) PL spectra of the Normal and Target films. Both films were kept under ambient conditions with a RH of 45% for 2000 h. d) Long-term stability of unencapsulated devices stored under ambient conditions of 25% RH and 25 °C. e) Long-term stability of unencapsulated devices at 25% RH, with temperature cycles ranging from 25 °C to 85 °C and back to 25 °C. f) Operational stability of the unencapsulated devices under continuous simulated AM1.5 illumination at the maximum power point and at \approx 50 °C in a N₂ glove box. g) OCVD curves of the Normal and Target PSCs. h) cs-TPT curves of the Normal and Target PSCs. i) Temperature-dependent conductivity measurements of Normal and Target perovskite films under ambient conditions with 45% RH and 25 °C.

improved photovoltaic performance compared to the Normal PSCs. In short, the observed PCE enhancement demonstrates that 2-HZP effectively improves device performance, with consistent efficacy across different device architectures, active areas, and perovskite compositions.

2.4. Stability Enhancement and Ion Migration Suppression

The introduction of 2-HZP can passivate adjacent $V_{\rm FA}$ and $V_{\rm I}$ defects and modulate the perovskite crystallization, which suggests potential enhancement in the device stability. To systematically investigate the influence of 2-HZP on device stability, aging experiments were conducted on perovskite precursor solutions, perovskite films, and devices under controlled environmental stressors. We first performed experiments by aging freshly prepared precursor solutions (Normal and Target samples) in ambi-

ent air with ~45% relative humidity (RH) under open-vial conditions. As illustrated in Figure S21 (Supporting Information), after 168 h, the Target solution remained visually unchanged, while the Normal solution exhibited a slight vellowing. This discoloration is primarily attributed to the degradation of PbI₂ and side reactions involving amine cations. The presence of 2-HZP helps mitigate these issues by forming hydrogen bonds with FA⁺, thereby stabilizing it, and by coordinating with Pb2+, which reduces the probability of decomposition. The humidity stability of perovskite film was evaluated by exposing perovskite films to 45% RH for 2000 h. Surface morphological evolution of the aged films was tracked. The SEM analysis (Figures 6a,b) demonstrates marked stability enhancement of the target film, which can be supported by the slight morphological changes. Furthermore, as shown in Figure 6c, PL measurements at the initial and final stages revealed distinct degradation behaviors in the Normal films, as evidenced by significant PL peak shifts. These shifts

15214095, 2025

, 40, Downloaded from https://advanced.onlinelibrary.viley.com/doi/10.1002/adma.202508643 by North China Electric Power University Beijing, Wiley Online Library on [14/10/2025]. See the Terms and Conditions (https://onlinelibrary.wiley.com/terms-and-conditions) on Wiley Online Library for rules of use; OA article are governed by the applicable Creative Commons License

are attributed to moisture-induced phase segregation resulting from partial perovskite decomposition, which leads to the local enrichment of FAPbI_3 domains after 2000 h of aging. $^{[38,39]}$ In contrast, Target films maintained stable spectral profiles without observable peak shifts. These measurements of SEM and PL conclusively demonstrate that 2-HZP modification substantially enhances the environmental stability of perovskite films.

After discussing the stability of the films, we also performed aging characterization on the devices. The evolution of PCE in unencapsulated devices was systematically monitored under ambient storage conditions (25% RH, 25 °C). The Target devices exhibited enhanced stability, retaining 93% of their initial PCE after 3000 h of aging, while the Normal devices maintained only 75% of their original efficiency (Figure 6d). The harsher conditions were also used to accelerate the device's aging. The devices were subjected to temperature cycling between 25 °C and 85 °C, with one cycle lasting 35 min. As shown in Figure 6e, after 150 cycles, the Target devices retained 90% of their initial PCE, while the Normal devices maintained only 67% of their initial PCE. We also conducted more rigorous stability tests, including thermal aging at 85 °C and continuous ultraviolet irradiation. As shown in Figures S22 and S23 (Supporting Information), after 336 h, the Target devices retained 92% and 96% of their initial efficiency, respectively, in contrast to the pronounced degradation observed in the Normal devices. Long-term operational stability was also characterized under continuous 1-sun illumination conditions in an N₂ environment. Impressively, as shown in Figure 6f, the Target PSC retained 93% of its initial PCE after 1700 h of operation, while the Normal PSC exhibited a significant decline after only 700 h.

The above aging experiment analysis demonstrates that 2-HZP significantly enhances the stability of both perovskite films and devices. The reason for the enhanced stability should primarily result from the defects passivation of 2-HZP, including the adjacent V_{FA} and V_I. The passivated defects may effectively suppress ion migration within the perovskite films. To gain deeper mechanistic insights, we examined the ion accumulation and migration dynamics in both Target and Normal devices using open-circuit photovoltage decay (OCVD) and Circuit-Switched Transient photoelectric technique (cs-TPT).[40,41] As depicted in Figure 6g, the OCVD kinetics exhibit distinct characteristics: the rapid decay phase (<1 ms) corresponds to free charge recombination, while the slower decay phase (>1 ms) is attributed to ion accumulation-induced recombination, directly reflecting the ion migration process. Notably, the Target device exhibits a significantly suppressed ion migration rate compared to the Normal device. To further evaluate ion accumulation under working conditions, we performed cs-TPT analysis. As illustrated in Figure 6h, the parameter V_r, which reflects the degree of ion accumulation in PSCs, shows a rising trend with increasing photovoltage (V_{ph}) . This indicates that the concentration of accumulated ions is positively correlated with the device's photovoltage. However, beyond a critical threshold (0.76 V for the Target device and 0.84 V for the Normal), ion accumulation saturates, likely due to the finite density of mobile ions under the given illumination conditions. This saturation behavior suggests that the total ion accumulation in the Target device is inherently lower than that in the Normal device, highlighting the impact of 2-HZP on mitigating excessive ion migration. Additionally, the active migration energy was

characterized through the temperature-dependent conductivity measurements of the Normal and Target devices. As revealed in Figure 6i, the active migration energy of the Normal device is 0.44 eV, while the corresponding value for the Target device is 0.91 eV. This increase in active migration energy further validates that the interaction between 2-HZP and the perovskite can effectively suppress ion migration within the devices, thereby enhancing the device stability.

3. Conclusion

In summary, our work revealed the mutual promotion mechanism of adjacent cation and anion vacancies in PSCs via DFT and AIMD calculations. Building upon this fundamental insight, we selected 2-HZP as an optimal additive to address adjacent defect passivation. Through theoretical calculations and experimental verification, we systematically demonstrated that 2-HZP achieves effective defects passivation through hydrogen-bond anchoring of FA⁺ and coordination-mediated V₁, while simultaneously regulating perovskite crystallization kinetics. Owing to 2-HZP's effective defects passivation, the inverted PSCs show an impressive efficiency of 26.28% with an aperture area of 0.08 cm² and 24.71% with an aperture area of 1 cm². Furthermore, the device can retain 93% of its initial efficiency after 1700 h of operation under 1-sun illumination and retain 90% of its initial efficiency after exposure to harsh thermal cycling. Our work revealed a clear inter-influence mechanism of adjacent cation and anion vacancies in perovskite and provided an effective passivation strategy, which provides guidelines for solving bottleneck issues regarding the perovskite defects, and more opportunities for developing commercially available PSCs.

4. Experimental Section

Materials: The materials used in this study have not been subjected to additional purification processes and include the following: FTO glass substrate (Suzhou ShangYang), MeO-4PACz (TCI, >99.0%), 2-hydrazinylpyrazine (Innochem, 95%), PbI₂ (TCI, 99.999%), PbCl₂ (Alfa, 99.999%), DMF, ACN and DMSO (Sigma–Aldrich, 99.9%), chlorobenzene (Sigma–Aldrich, 99.5%), isopropanol (Acros, 99.9%), FAI, MAI, MACI, CsI, PEAI, 4-MeO-PEAI, PCBM, tBP, Li-TSFI, Spiro and BCP (Xi'an Polymer Light Technology Corp).

Device Fabrication: For the fabrication of small-sized inverted perovskite solar cells: FTO substrates were initially ultrasonically cleaned for 15 min each in detergent, deionized water, ethanol, and again deionized water. A 0.45 mg mL $^{-1}$ MeO-4PACz solution was then spin-coated onto the cleaned substrates at 5000 rpm for 30 s, followed by a 15-min annealing at 100 °C. For the perovskite layer, a 1.5 m Cs $_{0.05}$ FA $_{0.85}$ MA $_{0.1}$ PbI $_{3}$ precursor (with 0.3 mol% 2-HZP) was prepared in a 1:4 DMSO/DMF solvent mixture, supplemented by 10 mol% MACI and 5 mol% PbCl $_{2}$, and spin-coated at 1000 rpm for 10 s and then 6000 rpm for 35 s. During the final 7 s, 220 µL chlorobenzene was dropped onto the film, which was subsequently dried at 100 °C for 25 min. A 2 mg mL $^{-1}$ PEAI solution was then spin-coated at 4000 rpm for 30 s and heated for 3 min for passivation. Next, a 20 mg mL $^{-1}$ PCBM solution in chlorobenzene was coated at 2000 rpm for 30 s, followed by a BCP layer (0.5 mg mL $^{-1}$) at 4000 rpm for 30 s. Finally, a 100 nm Ag electrode was deposited via thermal evaporation.

For the fabrication of 1 cm 2 inverted perovskite solar cells: The fabrication procedure was essentially the same as that for small-sized perovskite solar cells, but because of the increased device area, the volume of the anti-solvent (chlorobenzene) needs to be raised from 200 to 320 μ L.

For the fabrication of small-sized regular perovskite solar cells: Based on Huang et al.'s protocol, cleaned FTO substrates were immersed in a TiO $_2$ solution at 70 °C for 40 min. Perovskite layers were then formed using a one-step approach: a 1.54 M solution of FA $_{0.85}$ MA $_{0.1}$ Cs $_{0.05}$ Pbl $_3$ (with 0.3 mol% 2-HZP) supplemented by 10 mol% MACl was spin-coated at 4000 rpm for 18 s, with 900 μ L of diethyl ether added as an anti-solvent during the final 12 s of spin-coating. The films were then pre-annealed at 60 °C for 3 min and further heated at 130 °C for 15 min. A 16 mM 4-MeO-PEAI solution was spin-coated onto the FTO/TiO $_2$ /perovskite layer at 4000 rpm for 30 s, without additional annealing. Next, the hole-transport layer, consisting of spiro (72.3 mg), tBP (26.6 μ L), and Li-TFSI (18 μ L of a 520 mg mL $^{-1}$ solution in ACN) dissolved in 1 mL chlorobenzene, was deposited under the same spinning conditions. Finally, a 60 nm gold electrode was thermally evaporated onto the resulting substrate.

Characterization: In order to verify the interaction between perovskite and 2-HZP, Fourier-transform infrared spectroscopy (FTIR, PerkinElmer, Spectrum3) was employed. To verify the valence band changes of surface elements in perovskite film, X-ray photoelectron spectroscopy (XPS, Thermo Fisher Scientific ESCALAB 250Xi) characterization was employed. To characterize the surface morphology and crystallinity of the perovskite films, scanning electron microscopy (SEM, Hitachi S-4800) and X-ray diffraction (XRD, D8 Advance, Bruker) were employed. Photoluminescence (PL) mapping was carried out on a Nikon-ARSiMP-LSM-Kit-Legend Elite-USX laser confocal fluorescence lifetime imaging microscope using a 405 nm excitation source. Meanwhile, the carrier dynamics of the perovskite films were investigated through time-resolved photoluminescence (TRPL, FLS980). Transient absorption spectrometry (TAS) was performed by TA100 (Time-tech Spectra). In situ PL spectra were recorded by a commercialized dynamic spectrometer system.

The device performance was evaluated with a Keithley 2400 source meter under simulated AM 1.5 G illumination, using a mask area of 0.08 and 1 cm². The external quantum efficiency (EQE) and integrated current of the perovskite solar cells were measured using Enli Tech QE-R systems. Operational stability was tracked under LED illumination (AM 1.5 G) at 50 \pm 5 °C. For temperature cycling aging tests, a PL-80-2C (LAB COMPANION LTD) temperature and humidity chamber was used, cycling from 25 °C to 85 °C and back to 25 °C at 25% RH.

To investigate the ion migration activation energy, a vertical device was fabricated. The activation energy $(E_{\rm a})$ was obtained from the slope of the $\ln(\sigma T)^{-1}/kT$ plot, based on the temperature-dependent ion conductivity determined using the Nernst-Einstein equation: $\sigma(T) = (\sigma_0/T) \exp(-E_a/kT)$, where k was the Boltzmann constant, σ_0 was a constant, and T was the absolute temperature.

In the OCVD measurement, the device was illuminated with a continuous-wave light source (520 nm, Lambda Beam; RGB Photonics, Germany) until it reached its open-circuit voltage ($V_{\rm OC}$). Upon turning off the illumination, the photovoltage decay process was recorded using a digital oscilloscope. The cs-TPT measurement was built upon the OCVD setup and performed in two steps. First, during the OCVD process, the circuit was switched to a short-circuit state via a custom-built CMOS switch (switching speed <10 ns) to extract all free charges from the PSC device. Then, the circuit was reset to an open-circuit state, allowing the voltage recovery process of the PSC to be monitored. The maximum voltage recovery ($V_{\rm r, max}$) reflects the extent of ion accumulation at the interface.

Density Functional Theory Calculations: Density functional theory (DFT) calculations were performed using the Vienna Ab initio Simulation Package (VASP). [42,43] The exchange-correlation interactions were described by the Perdew-Burke-Ernzerhof (PBE) functional within the generalized gradient approximation (GGA) framework. [44,45] Core-valence electron interactions were modeled using the projected augmented wave (PAW) method. [46] A plane-wave energy cutoff of 400 eV was applied, and the Brillouin zone was sampled with a 2 \times 2 \times 1 Monkhorst-Pack k-point grid. Structural optimizations proceeded until the energy and force were converged to 1.0 \times 10 $^{-4}$ eV and 0.05 eV Å $^{-1}$, respectively.

The adsorption energy (E_{ads}) was defined as:

$$E_{ads} = E_{complex} - E_{slab} - E_{cluster}$$
 (1)

where slab and cluster refer to the metal surface and adsorbate molecule, respectively.

Ab Initio Molecular Dynamics Calculations: CP2K[⁴⁷] was employed to carry out the theoretical calculations in the framework of density functional theory (DFT). In CP2K/Quickstep, the electron density was described through both localized Gaussian and plane-wave basis sets. For the Gaussian-based Kohn-Sham orbitals, a library of contracted, molecularly optimized valence double-zeta plus polarization basis sets was employed, [⁴⁸] while the complementary plane-wave basis for the electron density featured a cutoff of 400 Rydberg. Structural relaxation was performed using the Perdew–Burke–Ernzerhof (PBE) functional [⁴⁹] and included dispersion corrections based on the Grimme D3 approach. [⁵⁰] To sample the bulk solution structures, canonical ensemble (NVT) conditions were enforced using a Nose-Hoover thermostat at 298.15 K, with a 1.0 fs time step.

Supporting Information

Supporting Information is available from the Wiley Online Library or from the author.

Acknowledgements

This work is supported partially by the Beijing Natural Science Foundation (Z240024), National Natural Science Foundation of China (Grant nos. 52232008, 52402254, 52102245, and 22409061), Beijing Nova Program (20220484016), Young Elite Scientists Sponsorship Program by CAST (2022QNRC001), Huaneng Group Headquarters Science and Technology Project (HNKJ20-H88), the Fundamental Research Funds for the Central Universities (2023MS042, 2024MS036, 2023MS047, 2024MS039, and 2024JC005) and the NCEPU "Double First-Class" Program.

Conflict of Interest

The authors declare no conflict of interest.

Data Availability Statement

The data that support the findings of this study are available from the corresponding author upon reasonable request.

Keywords

defect passivation, high efficiency, ion migration, perovskite solar cells, stability

Received: May 7, 2025 Revised: July 1, 2025 Published online: August 7, 2025

- [1] H. Zai, P. Yang, J. Su, R. Yin, R. Fan, Y. Wu, X. Zhu, Y. Ma, T. Zhou, W. Zhou, Y. Zhang, Z. Huang, Y. Jiang, N. Li, Y. Bai, C. Zhu, Z. Huang, J. Chang, Q. Chen, Y. Zhang, H. Zhou, Science 2025, 387, 186.
- [2] E. Ugur, A. A. Said, P. Dally, S. Zhang, C. E. Petoukhoff, D. Rosas-Villalva, S. Zhumagali, B. K. Yildirim, A. Razzaq, S. Sarwade, A. Yazmaciyan, D. Baran, F. Laquai, C. Deger, I. Yavuz, T. G. Allen, E. Aydin, S. De Wolf, Science 2024, 385, 533.
- [3] T. Duan, S. You, M. Chen, W. Yu, Y. Li, P. Guo, J. J. Berry, J. M. Luther, K. Zhu, Y. Zhou, *Science* **2024**, *384*, 878.



www.advancedsciencenews.com



www.advmat.de

15214095, 2025

onlinelibrary.wiley.com/doi/10.1002/adma.202508643 by North China

Electric Power University Beijing, Wiley Online Library on [14/10/2025]. See the Terms

on Wiley Online Library for rules

of use; OA

articles are governed by the applicable Creative Commons

- [4] S. Liu, J. Li, W. Xiao, R. Chen, Z. Sun, Y. Zhang, X. Lei, S. Hu, M. Kober-Czerny, J. Wang, F. Ren, Q. Zhou, H. Raza, Y. Gao, Y. Ji, S. Li, H. Li, L. Qiu, W. Huang, Y. Zhao, B. Xu, Z. Liu, H. J. Snaith, *Nature* 2024, 632, 536.
- [5] Y. Wang, R. Lin, C. Liu, X. Wang, C. Chosy, Y. Haruta, A. D. Bui, M. Li, H. Sun, X. Zheng, H. Luo, P. Wu, H. Gao, W. Sun, Y. Nie, H. Zhu, K. Zhou, H. T. Nguyen, X. Luo, L. Li, C. Xiao, M. I. Saidaminov, S. D. Stranks, L. Zhang, H. Tan, *Nature* 2024, 635, 867.
- [6] J. Chen, X. Wang, T. Wang, J. Li, H. Y. Chia, H. Liang, S. Xi, S. Liu, X. Guo, R. Guo, Z. Jia, X. Yin, Q. Zhou, Y. Wang, Z. Shi, H. Zhou, D. Lai, M. Zhang, Z. Xing, W. R. Leow, W. Yan, Y. Hou, Nat. Energy 2025, 10, 181
- [7] H. Zhou, K. Cai, S. Yu, Z. Wang, Z. Xiong, Z. Chu, X. Chu, Q. Jiang, J. You, Nat. Commun. 2024, 15, 6679.
- [8] H. Zhang, L. Pfeifer, S. M. Zakeeruddin, J. Chu, M. Grätzel, Nat. Rev. Chem. 2023, 7, 632.
- [9] Y. Yuan, J. Huang, Acc. Chem. Res. 2016, 49, 286.
- [10] J. Min, Y. Choi, D. Kim, T. Park, Adv. Energy Mater. 2023, 14, 2302659.
- [11] C. Liu, Y. Yang, H. Chen, J. Xu, A. Liu, A. S. R. Bati, H. Zhu, L. Grater, S. S. Hadke, C. Huang, V. K. Sangwan, T. Cai, D. Shin, L. X. Chen, M. C. Hersam, C. A. Mirkin, B. Chen, M. G. Kanatzidis, E. H. Sargent, Science 2023, 382, 810.
- [12] Q. Cai, Q. Tan, J. He, S. Tang, Q. Sun, D. He, T. Cheng, G. Ma, J. Huang, G. Su, C. Chen, H. Gu, B. Wang, J. Fan, G. Xing, Z. He, *Joule* 2025, 9, 101880.
- [13] S. Du, H. Huang, Z. Lan, P. Cui, L. Li, M. Wang, S. Qu, L. Yan, C. Sun, Y. Yang, X. Wang, M. Li, *Nat. Commun.* 2024, 15, 5223.
- [14] L. Yan, H. Huang, P. Cui, S. Du, Z. Lan, Y. Yang, S. Qu, X. Wang, Q. Zhang, B. Liu, X. Yue, X. Zhao, Y. Li, H. Li, J. Ji, M. Li, *Nat. Energy* 2023, 8, 1158.
- [15] Z. Xiong, Y. S. Jeon, H. Wang, G. Fu, S. H. Cho, S. J. Chang, P. A. van Aken, N. G. Park, Adv. Mater. 2025, 37, 2413712.
- [16] H. S. Kim, N. G. Park, Adv. Energy Mater. 2025, 15, 2400089.
- [17] W. Zhou, X. Chen, R. Zhou, H. Cai, Y. Wang, T. Zhang, Z. Zheng, F. Gao, Y. Zhang, H. Yan, Small 2024, 20, 2310368.
- [18] Y. Ding, B. Ding, P. Shi, J. Romano-deGea, Y. Li, R. C. Turnell-Ritson, O. A. Syzgantseva, I. Yavuz, M. Xia, R. Yu, M. A. Syzgantseva, J. N. Audinot, X. Miao, X. Liao, J. Li, P. Dörflinger, V. Dyakonov, C. Liu, Y. Yang, L. Tao, K. G. Brooks, A. Slonopas, J. Pan, L. Zhang, Q. An, Y. Rong, J. Peng, L. Ding, E. Shi, L. Mai, et al., Science 2024, 386, 531.
- [19] L. Tian, E. Bi, I. Yavuz, C. Deger, Y. Tian, J. Zhou, S. Zhang, Q. Liu, J. Shen, L. Yao, K. Zhao, J. Xu, Z. Chen, L. Xiao, Z. Yang, P. Shi, X. Zhang, S. Wang, S. Chu, M. Haider, J. Xue, R. Wang, Nat. Photonics 2025, 19, 479.
- [20] Y. Liang, F. Li, X. Cui, C. Stampfl, S. P. Ringer, X. Yang, J. Huang, R. Zheng, Sci. Adv. 2025, 11, ads7054.
- [21] F. Li, X. Deng, Z. Shi, S. Wu, Z. Zeng, D. Wang, Y. Li, F. Qi, Z. Zhang, Z. Yang, S. H. Jang, F. R. Lin, S. W. Tsang, X. K. Chen, A. K. Y. Jen, *Nat. Photonics* 2023, 17, 478.
- [22] Y. Xu, X. Guo, Z. Lin, Q. Wang, J. Su, J. Zhang, Y. Hao, K. Yang, J. Chang, Angew. Chem., Int. Ed. 2023, 62, 202306229.
- [23] X. Chen, Q. Wang, H. Wei, J. Yang, Y. Yao, W. Tang, W. Qiu, X. Xu, L. Song, Y. Wu, Q. Peng, Energy Environ. Sci. 2024, 17, 7342.
- [24] M. Azam, Y. Ma, B. Zhang, X. Shao, Z. Wan, H. Zeng, H. Yin, J. Luo, C. Jia, Nat. Commun. 2025, 16, 602.

- [25] X. Zhao, D. Wu, H. Yan, P. Cui, Y. Qiu, B. Fan, X. Yue, L. Li, M. Li, Small 2024, 21, 2408606.
- [26] X. Zhao, Y. Qiu, M. Wang, D. Wu, X. Yue, H. Yan, B. Fan, S. Du, Y. Yang, Y. Yang, D. Li, P. Cui, H. Huang, Y. Li, N. G. Park, M. Li, ACS Energy Lett. 2024, 9, 2659.
- [27] Y. Shao, Z. Xiao, C. Bi, Y. Yuan, J. Huang, Nat. Commun. 2014, 5, 5784.
- [28] N. Li, S. Tao, Y. Chen, X. Niu, C. K. Onwudinanti, C. Hu, Z. Qiu, Z. Xu, G. Zheng, L. Wang, Y. Zhang, L. Li, H. Liu, Y. Lun, J. Hong, X. Wang, Y. Liu, H. Xie, Y. Gao, Y. Bai, S. Yang, G. Brocks, Q. Chen, H. Zhou, Nat. Energy 2019, 4, 408.
- [29] C. Fei, A. Kuvayskaya, X. Shi, M. Wang, Z. Shi, H. Jiao, T. J. Silverman, M. Owen-Bellini, Y. Dong, Y. Xian, R. Scheidt, X. Wang, G. Yang, H. Gu, N. Li, C. J. Dolan, Z. J. D. Deng, D. N. Cakan, D. P. Fenning, Y. Yan, M. C. Beard, L. T. Schelhas, A. Sellinger, J. Huang, Science 2024, 384, 1126
- [30] H. Yan, X. Zhao, H. Huang, D. Wu, P. Zhu, D. Li, B. Fan, Y. Qiu, Y. Yang, Q. Geng, P. Cui, Y. Yang, Z. Lan, M. Li, Adv. Energy Mater. 2025, 15, 2403200.
- [31] X. Zhuang, D. Zhou, Y. Jia, S. Liu, J. Liang, Y. Lin, H. Hou, D. Qian, T. Zhou, X. Bai, H. Song, Adv. Mater. 2024, 36, 2403257.
- [32] D. Wang, H. Guo, X. Wu, X. Deng, F. Li, Z. Li, F. Lin, Z. Zhu, Y. Zhang, B. Xu, A. K. Y. Jen, Adv. Funct. Mater. 2022, 32, 2107359.
- [33] J. I. Khan, Y. Yang, J. R. Palmer, S. B. Tyndall, S. Chaudhuri, C. Liu, L. Grater, J. D. North, B. Chen, R. M. Young, G. C. Schatz, M. R. Wasielewski, M. G. Kanatzidis, D. F. Swearer, E. H. Sargent, *Matter* 2024, 7, 2536.
- [34] M. Chen, Y. Li, Z. Zeng, M. Liu, T. Du, X. Huang, L. Bi, J. Wang, W. Jiang, Y. An, S. W. Tsang, J. Yin, S. Wu, A. K. Y. Jen, *Energy Environ. Sci.* 2024, 17, 9580.
- [35] H. Li, C. Zhang, C. Gong, D. Zhang, H. Zhang, Q. Zhuang, X. Yu, S. Gong, X. Chen, J. Yang, X. Li, R. Li, J. Li, J. Zhou, H. Yang, Q. Lin, J. Chu, M. Grätzel, J. Chen, Z. Zang, Nat. Energy 2023, 8, 946.
- [36] C. Luo, G. Zheng, F. Gao, X. Wang, Y. Zhao, X. Gao, Q. Zhao, *Joule* 2022. 6, 240.
- [37] H. Huang, P. Cui, Y. Chen, L. Yan, X. Yue, S. Qu, X. Wang, S. Du, B. Liu, Q. Zhang, Z. Lan, Y. Yang, J. Ji, X. Zhao, Y. Li, X. Wang, X. Ding, M. Li, *Joule* 2022, 6, 2186.
- [38] Y. Yang, Q. Chang, J. Su, L. Chao, Y. Wang, Z. Dai, X. Huang, S. Nie, P. Guo, J. Yin, Z. Liu, Y. H. Lin, A. K. Y. Jen, R. Chen, H. Wang, Adv. Mater. 2025, 37, 2416513.
- [39] C. Ma, F. T. Eickemeyer, S. H. Lee, D. H. Kang, S. J. Kwon, M. Grätzel, N. G. Park, *Science* **2023**, *379*, 173.
- [40] S. Qu, H. Huang, J. Wang, P. Cui, Y. Li, M. Wang, L. Li, F. Yang, C. Sun, Q. Zhang, P. Zhu, Y. Wang, M. Li, Angew. Chem., Int. Ed. 2025, 137, 202415949.
- [41] Y. Li, S. Qu, J. Wu, H. Fang, N. Liu, P. Cui, M. Li, X. Ai, J. Phys. Chem. Lett. 2024, 15, 11903.
- [42] G. Kresse, J. Hafner, Phys. Rev. B 1993, 47, 558.
- [43] G. Kresse, J. Hafner, Phys. Rev. B 1994, 49, 14251.
- [44] J. P. Perdew, K. Burke, M. Ernzerhof, Phys. Rev. Lett. 1996, 77, 3865.
- [45] G. Kresse, D. Joubert, Phys. Rev. B 1999, 59, 1758.
- [46] P. E. Blöchl, Phys. Rev. B 1994, 50, 17953.
- [47] www.cp2k.org, J. Chem. Phys. 2020, 152, 194103.
- [48] V. Vande, J. J. Hutter, J. Chem. Phys. 2007, 127, 114105.
- [49] P. E. Blöchl, Phys. Rev. B 1994, 50, 17953.
- [50] S. Grimme, S. Ehrlich, L. Goerigk, J. Comput. Chem. 2011, 32, 1456.